

A computerized scheme for lung nodule detection in multiprojection chest radiography

Wei Guo

Carl E. Ravin Advanced Imaging Laboratories, Department of Radiology, Duke University Medical Center, Durham, North Carolina 27705 and College of Information Science and Engineering, Northeastern University, Shenyang, Liaoning 110004 China

Qiang Li^{a)}

Carl E. Ravin Advanced Imaging Laboratories, Department of Radiology, Duke University Medical Center, Durham, North Carolina 27705

Sarah J. Boyce

Carl E. Ravin Advanced Imaging Laboratories, Department of Radiology, Duke University Medical Center, Durham, North Carolina 27705 and Department of Biomedical Engineering, University of North Carolina, Chapel Hill, North Carolina 27599

H. Page McAdams

Carl E. Ravin Advanced Imaging Laboratories, Department of Radiology, Duke University Medical Center, Durham, North Carolina 27705

Junji Shiraishi

Faculty of Life Sciences, Kumamoto University, 4-24-1 Kuhonji, Kumamoto 962-0976, Japan

Kunio Doi

Kurt Rossmann Laboratories for Radiologic Image Research, Department of Radiology, The University of Chicago, Chicago, Illinois 60637

Ehsan Samei

Carl E. Ravin Advanced Imaging Laboratories, Department of Radiology, Duke University Medical Center, Durham, North Carolina 27705 and Departments of Physics, Biomedical Engineering, Electrical and Computer Engineering, and Medical Physics, Duke University, Durham, North Carolina 27705

(Received 15 September 2011; revised 9 December 2011; accepted for publication 16 January 2012; published 20 March 2012)

Purpose: Our previous study indicated that multiprojection chest radiography could significantly improve radiologists' performance for lung nodule detection in clinical practice. In this study, the authors further verify that multiprojection chest radiography can greatly improve the performance of a computer-aided diagnostic (CAD) scheme.

Methods: Our database consisted of 59 subjects, including 43 subjects with 45 nodules and 16 subjects without nodules. The 45 nodules included 7 real and 38 simulated ones. The authors developed a conventional CAD scheme and a new fusion CAD scheme to detect lung nodules. The conventional CAD scheme consisted of four steps for (1) identification of initial nodule candidates inside lungs, (2) nodule candidate segmentation based on dynamic programming, (3) extraction of 33 features from nodule candidates, and (4) false positive reduction using a piecewise linear classifier. The conventional CAD scheme processed each of the three projection images of a subject independently and discarded the correlation information between the three images. The fusion CAD scheme included the four steps in the conventional CAD scheme and two additional steps for (5) registration of all candidates in the three images of a subject, and (6) integration of correlation information between the registered candidates in the three images. The integration step retained all candidates detected at least twice in the three images of a subject and removed those detected only once in the three images as false positives. A leave-one-subject-out testing method was used for evaluation of the performance levels of the two CAD schemes.

Results: At the sensitivities of 70%, 65%, and 60%, our conventional CAD scheme reported 14.7, 11.3, and 8.6 false positives per image, respectively, whereas our fusion CAD scheme reported 3.9, 1.9, and 1.2 false positives per image, and 5.5, 2.8, and 1.7 false positives per patient, respectively. The low performance of the conventional CAD scheme may be attributed to the high noise level in chest radiography, and the small size and low contrast of most nodules.

Conclusions: This study indicated that the fusion of correlation information in multiprojection chest radiography can markedly improve the performance of CAD scheme for lung nodule detection. © 2012 American Association of Physicists in Medicine. [<http://dx.doi.org/10.1118/1.3694096>]

I. INTRODUCTION

Lung cancer is the leading cause of cancer-related mortality; American Cancer Society estimated that 157 300 lung cancer patients died in the United States in 2010.¹ One of the reasons for this high mortality is that many patients present with advanced-stage disease, and thus miss the best opportunity of potentially curative surgery. Some evidence suggests that the early detection of lung cancer may decrease mortality, with greater than 90% ten-year survival after the surgical resection of early-stage lung cancers.² Thus, the early diagnosis and treatment of lung cancers is the key to improving the survival rate for patients with lung cancer.

Because of its simplicity, low cost, and low x-ray dose, chest radiography has been the most commonly used imaging technique for lung cancer screening. However, in chest radiography, the normal anatomic structures (such as rib, mediastinum, and heart) may obscure lung cancer. Therefore, the sensitivity and specificity for screening lung cancer in chest radiography are very low.^{3,4} As the computed tomography (CT) has advanced rapidly, more and more hospitals utilize CT to screen lung cancers. The National Lung Screening Trial,⁵ a clinical study sponsored by the National Cancer Institute, showed that 20% fewer lung cancer deaths have been observed among those who were screened with low-dose spiral CT than those with chest radiography. However, widespread utilization of CT as a screening tool for lung cancer is still a highly controversial issue⁶ because of the high radiation dose and high cost.

Multiprojection chest radiography has been proposed to improve the detection performance of early-stage lung cancer without significant increase in the radiation dose levels.⁷⁻⁹ Multiprojection chest radiography acquires multiple radiographic images of the same patient at multiple angles by moving an x-ray tube. Because the projection images at different angles provide different geometrical perspectives, they can be utilized to reduce the influence of normal anatomical structures, and to detect some nodules missed in the standard chest radiography.

A multiprojection chest radiography system¹⁰ was designed and developed in the Department of Radiology at Duke University and is currently under clinical evaluation. This system was modified from a standard x-ray system, in which the x-ray tube can move along the horizontal and vertical axes. Samei *et al.*¹¹ developed a computer-aided diagnostic (CAD) scheme to detect simulated nodules in an anthropomorphic chest phantom based on this imaging system. Compared to a signal-view CAD, this CAD scheme improved the positive predictive value by 140%.

The CAD scheme mentioned above was based on two projection images. In this study, we horizontally moved the x-ray tube to acquire a PA image and two images at oblique views of $\pm 3^\circ$ for each subject, and employed these three images to detect nodules. Preliminary results of observer study indicated that the multiprojection chest radiography achieved a sensitivity of 86% compared to a sensitivity of 71% for the PA view only, and the total number of false positives was reduced by 35%. Therefore, the multiprojection

chest radiography can improve the performance of nodule detection in clinical practice.

The purpose of this study was to verify that the multiprojection chest radiography can also improve the performance of a CAD scheme for lung nodule detection. We developed a conventional CAD scheme and a new fusion CAD scheme to detect lung nodules. The conventional CAD scheme processed each of the three images of a subject independently and discarded the correlation information between the three images, as other CAD schemes did.¹²⁻²² The fusion CAD scheme included the conventional CAD scheme and two additional steps for registering all nodule candidates of a subject and integrating correlation information between the registered candidates to reduce false positives.

II. MATERIALS AND METHODS

II.A. Image database

This study was approved by IRB at Duke University. The data were clinically obtained using a multiprojection chest radiography equipment developed in the Department of Radiography at Duke University.¹⁰ Figure 1 shows the schematic geometry for the acquisition of multiprojection chest radiography. The multiprojection chest radiography of each subject comprised of three images, including a PA image and two images acquired at oblique views of $\pm 3^\circ$; they were acquired in a continuous acquisition mode with the tube moving speed of 2.5 cm/s. The detector was an amorphous silicon indirect flat-panel sensor (Paxscan, 4030CB series, Varian Medical Systems, Palo Alto, CA). The tube voltage was fixed at 120 kVp, and the tube exposure time product was varied between 1.25 and 6.40 mAs depending on the patient size. The radiation dose for acquiring each of the three projection images was approximately a third of that for acquiring a standard PA radiograph. Therefore, the total radiation dose of the multiprojection radiography was approximately equal to that of a standard PA radiograph. The source-to-image distance was 200 cm, and the center of the x-ray beam was 2.5 cm in front of the detector. The image had a pixel size of 0.194 mm and a matrix size of 2048×1536 . Compared with the size of pixels in the original image, the size of a nodule was very large. Therefore, we resampled the multiprojection chest radiography by averaging 16 pixels in a 4×4 region to reduce the processing time. The resampled image had a pixel size of 0.776 mm and a

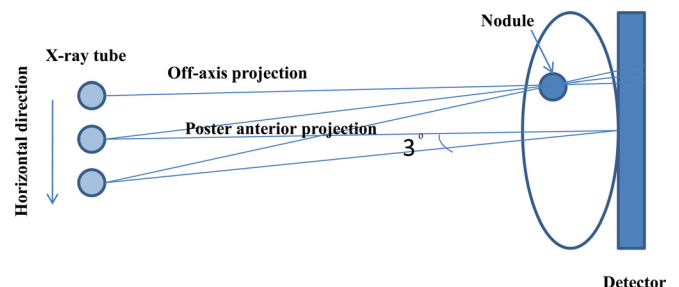


FIG. 1. The schematic geometry for the acquisition of multiprojection images.

matrix size of 512×374 . In the resampled images, a nodule still contained many pixels for us to reliably detect it.

Our database consisted of 59 subjects, including 43 subjects with 45 nodules ranging from 5 to 20 mm in diameter and 16 subjects without nodules. The 45 nodules included 7 real and 38 simulated ones generated by use of an algorithm developed by Alessandro *et al.*²⁴ For simulated nodules, the truth was known a priori per insertion of the simulated nodules in the chest images. For cases with real nodules, the truth was established by confirming the presence of the nodules with CT images of the subjects.

For both simulated and real nodules, the nodules as depicted in chest radiographs were reexamined by an experienced chest radiologist and were scored according to their subtlety from 1 (too faint-subtle) to 5 (too apparent). Only nodules scored between 2 and 4 were judged to be at the proper level of subtlety to be incorporated in the study. The subtlety scores of all the seven real nodules were between 2 and 4. The subtlety scores for some simulated nodules were initially either 1 or 5. For these simulated nodules with a score of 1 or 5, each of them was recreated until its score was between 2 and 4. We employed simulated nodules in this study as the number of real nodules was limited.

II.B. Identification of initial nodule candidates

Figure 2 is the diagrams of our conventional CAD scheme and fusion CAD scheme for lung nodule detection. The conventional CAD scheme consisted of four steps in the top of the Fig. 2, and the fusion CAD scheme included two additional steps in the bottom of Fig. 2.

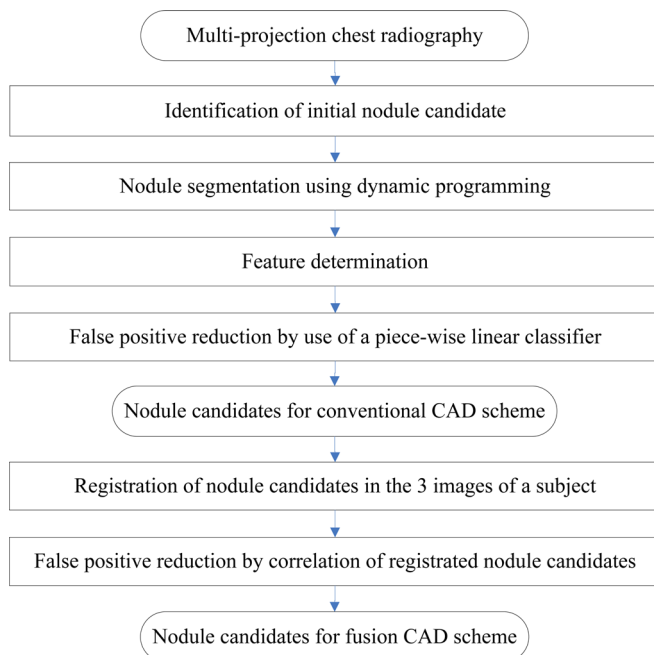


FIG. 2. Overall schemes of the conventional CAD scheme and the fusion CAD scheme for lung nodule detection on multiprojection chest radiography.

II.B.1. Lung segmentation and nodule enhancement

We first employed an existing profile analysis algorithm developed in the Department of Radiography at Chicago University^{25,26} for accurate delineation of lung boundaries. The top edges of lungs were identified by analyzing the second derivative of vertical profiles of the chest images, and the left and right ribcage edges were identified by analyzing the second derivative of horizontal profiles of the images.²⁵ Then, the right and left mediastinum boundaries were determined by analyzing the edge gradient in the mediastinum regions.²⁶ Finally, the lung areas were determined by using the delineated ribcage edges and the right and left mediastinum boundaries.

Because the shapes of most nodules can be approximated by Gaussian functions, we employed two Difference of Gaussian (DoG) filters¹¹ to enhance relatively small and large nodules. The output of a DoG filter was the difference between two Gaussian filters with two different scales. The scales (the sigmas in Gaussian functions) are the important parameters for enhancing nodules with specific sizes. In this study, we empirically employed a set of scales (2.4 and 3.6 mm) for enhancing small nodules, and another set (4.0 and 6.0 mm) for enhancing large nodules. In the nodule-enhanced image, the circular objects, such as nodules, were enhanced considerably, and objects of other shapes were not well enhanced. Therefore, the nodules could be detected more reliably in the enhanced images than in the original images. Figure 3(a) is an original PA image of a subject with a nodule indicated by a circle. Figures 3(b) and 3(c) show the nodule-enhanced images by use of the small and large scales, respectively.

II.B.2. Segmentation of initial nodule candidate

Because the contrast of nodules varies from one nodule to another, a fixed threshold would not provide a good performance for detecting nodules. Therefore, a multiple thresholding technique was employed to segment the nodules with different contrast. First, the gray values of a nodule-enhanced image were linearly transformed to the range between 0 and 1023. An empirical initial threshold of 900 was then used to segment the nodule-enhanced image, and a connected-component labeling algorithm was employed to identify all segmented components inside lungs. The labeled components with areas between 10 and 100 pixels ($7.8\text{--}77.6\text{ mm}^2$) were retained as initial nodule candidates, and other labeled components were discarded. The above process provided a binary image with identified nodule candidates. Please note that the areas of nodules in the nodule-enhanced image appeared smaller than their actual sizes, and that the very large nodules would be detected at certain thresholds. Finally, we decreased the threshold by a step of 5, and repeated the above procedure until one of two conditions was met (a) the threshold was less than 400 and (b) the total number of the pixels whose gray scale values were greater than the threshold was larger than 90% of the entire image. We obtained a binary image at each threshold level. The time to segment an image by using the multiple thresholding

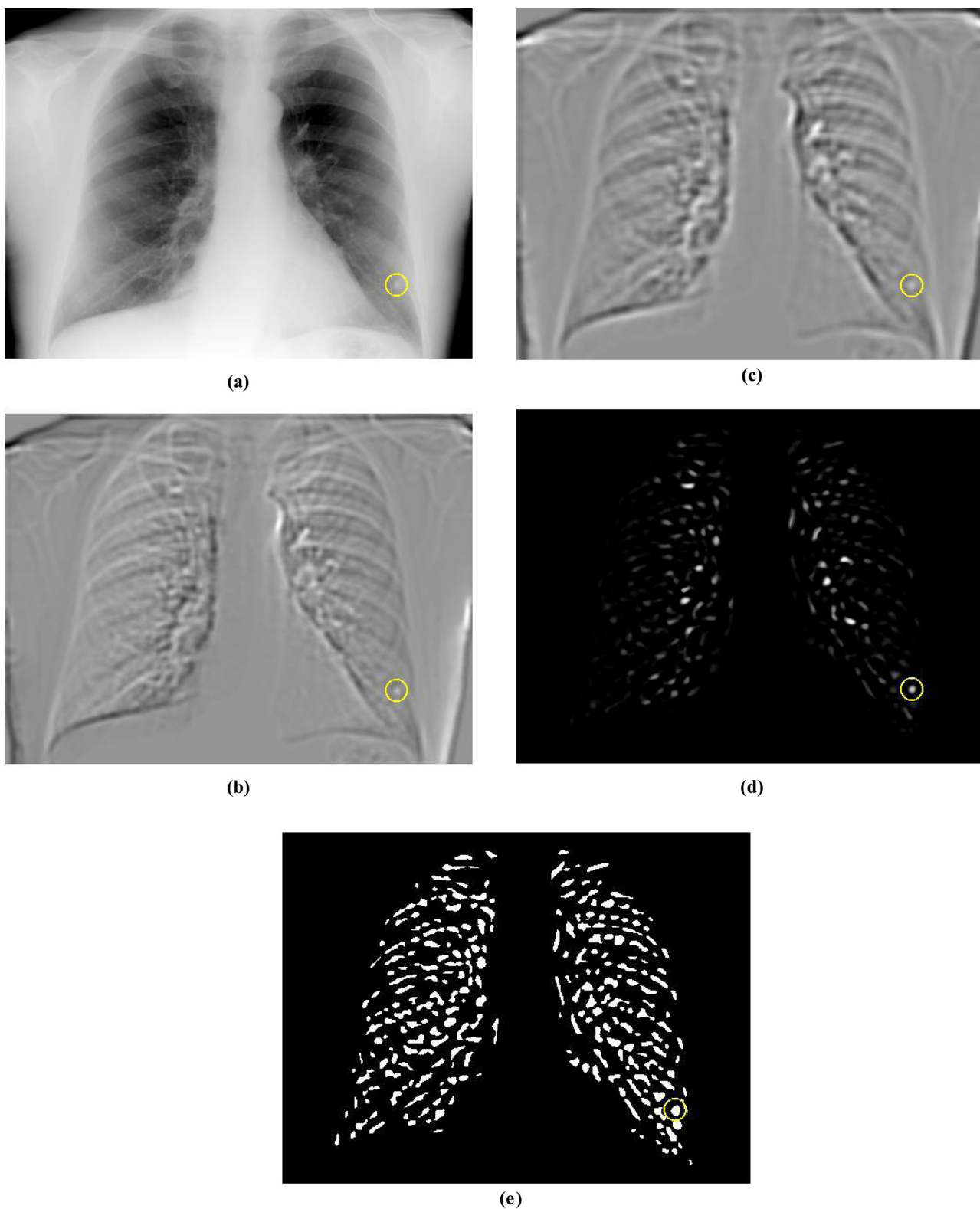


FIG. 3. Identification of initial nodule candidates. (a) An original PA image of a subject with a nodule indicated by a circle, (b) nodule-enhanced image with a small scale, (c) nodule-enhanced image with a large scale, (d) sum image of multiple binary images obtained by use of multithreshold segmentation of the two nodule-enhanced images in (b) and (c), and (e) initial nodule candidates.

technique is about 6 s on a PC with 2.66 GHz Intel Core 2 CPU and 3GB RAM using MATLAB programming language.

A sum image was determined by adding corresponding pixels in all binary images of the two nodule-enhanced

images. In the sum image, the value of each pixel indicated the times that it was identified as a pixel in an initial nodule candidate in the binary images. If a pixel in the sum image was equal to or larger than 3, it was considered as a pixel in

the initial nodule candidate. Figures 3(d) and 3(e) show the sum image and the image of initial nodule candidates, respectively. Although the number of false positives in the sum image was large, the shape of most false positives was different from that of nodules, and could be removed later using simple features (such as circularity).

II.C. Segmentation of nodule candidates based on dynamic programming

Because the shape of a nodule in the nodule-enhanced image was a little different from the actual shape in the original image, we attempted to segment nodule candidates accurately in the original images by use of dynamic programming.

II.C.1. Polar-coordinate transformation

First, a small region of interest (ROI) of 41×41 pixels ($31.8 \times 31.8 \text{ mm}^2$) was defined at the center of each nodule candidate. To minimize the effect of background trend, a bilinear function (plane) was fitted to all pixels in the small ROI image, and then the corresponding value of bilinear function was subtracted from the pixel value of the original ROI image. Figures 4(a) and 4(b) show the original ROI image of a nodule and the image after background trend removal, respectively.

Sixty radial lines (6° apart) of 21 pixels (16.3 mm) long were evenly drawn from the center of the ROI of a nodule candidate. We arranged all pixels on the 60 radial lines sequentially to form a transformed polar-coordinate image as shown in Fig. 4(c). The outline of a nodule was approximately a horizontal curve in the transformed image, and could be accurately delineated by use of dynamic programming.

II.C.2. Dynamic programming

II.C.2.1. Forward calculation of cumulative cost. Dynamic programming is an optimization method, and often used for tracing the optimal outline of an object.^{27,28} In this study, we employed dynamic programming to determine the outlines of nodule candidates in the multiprojection chest radiography. The optimal outline consisted of 60 edge points (one

and only one edge point on each of sixty columns) in the polar-coordinate image shown in Fig. 4(c). The optimal outline connecting the 60 edge points would have the lowest cumulative cost compared with all other possible outlines.

The cumulative cost of a nodule outline was defined as the sum of local costs of all edge points on the outline. The local cost was defined as the weighted sum of the internal and external costs. We empirically set the weighing factors of the internal and external costs to 30 and 1, respectively. The internal cost measured the smoothness between edge points on the adjacent columns, and it was defined as the ratio of the difference to the sum of the y-coordinates of the two edge points on two adjacent columns. The external cost measured the strength of change in gray scale at an edge point, and it was defined as the difference in gray scale between the two pixels above and below the edge point of interest in the polar-coordinate image.

The cumulative cost of an outline was dynamically calculated column-by-column from the first column to the last column in the polar-coordinate image.²⁸ The cumulative cost of a pixel on the first column in the polar-coordinate image consisted of only the external cost of the pixel, and the cumulative cost of a pixel on the i th column was defined as the sum of the cumulative cost at the $(i - 1)$ th column and the local cost at the pixel.

Because the previous column of the first column was actually the sixtieth column, and the smoothness between these two columns was not included in the internal cost, a large “jump” would occur between two edge points on the sixtieth and first columns. In order to overcome this problem, we extended the polar-coordinate image by repeating the original polar-coordinate image twice, as shown in Fig. 4(d). The optimal outline of the nodule candidate was obtained from the second half of the extended polar-coordinate image.

II.C.2.2. Backward search of the optimal outline. After the calculation of the cumulative costs of all points on the last column, a backward search strategy²⁸ was employed to determine the optimal outline. First, we selected the pixel with the lowest cumulative cost on the last column. From the

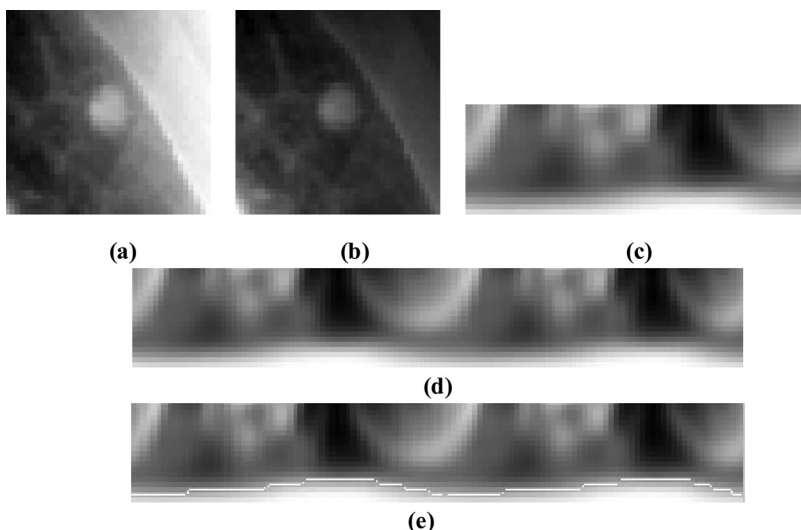


FIG. 4. Major steps of accurate nodule segmentation using dynamic programming. (a) Original small image of a nodule, (b) image after background trend removal, (c) polar-coordinate image, (d) extended polar-coordinate image, and (e) segmentation result in the extended polar-coordinate image.

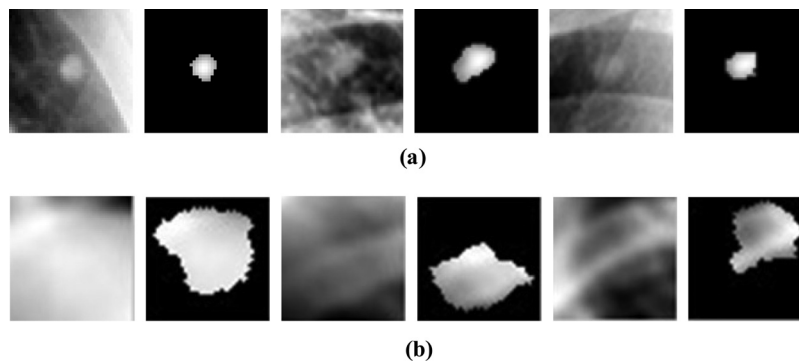


FIG. 5. The original and segmented images of (a) three nodules and (b) three non-nodules.

selected pixel on the last column, we traced the outline one step backward to the “optimal” edge point on the second column from the last. This procedure was repeated to find the pixels on the optimal outline all the way back to the first column. The white curve in Fig. 4(e) is the optimal outline obtained by dynamic programming.

The pixels on the optimal outline of a nodule candidate were then transformed back to the small ROI image, and adjacent edge pixels on the optimal outline were connected by straight lines to form a closed and continuous curve. Figure 5 shows the original and segmented images of three nodules and three false positives. The first nodule was the one shown in Fig. 4. It is apparent from Fig. 5 that dynamical programming provided quite accurate segmentation results for nodules, and less accurate segmentation results for false positives due to their fuzzy boundaries. The large difference in segmented shape between nodules and false positives would enable us to remove most false positives while maintaining a relatively high sensitivity.

II.D. Feature determination

II.D.1. Features based on gray scale and edge gradient of nodule candidates

We determined 33 features based on gray scale, edge gradient, shape, symmetry, and locations of nodule candidates as shown in Table I. The features based on gray scale included the mean and standard deviation of the gray scale and the mean of the edge gradient for the pixels inside the initially detected regions and accurately segmented regions

of nodule candidates. The interval for calculating edge gradients was 2 pixels.

II.D.2. Features based on shape of nodule candidates

We determined as features the degree of circularity, compactness, area, eccentricity, effective diameter, the ratio of the length of the minor axis to the length of the major axis of the ellipse that had the same second moments as the region of the nodule candidate, the logarithm of the first three moment invariants, and the maximum absolute value of the Fourier descriptors. The definitions and meanings of these features are provided in Ref. 29.

We found that the last four moment invariants represented very subtle details, and lacked power to represent the main characteristics of nodule candidates. Thus, they were not able to well distinguish nodules from false positives, and were discarded. The logarithm was used to reduce the extremely large dynamic range of moment invariants. The maximum absolute value of the Fourier descriptors was used for its excellent ability in representing the shape of nodule candidates.

II.D.3. Features based on symmetry of nodule candidates

Most segmented areas of nodules were in the middle of the images, and were approximately symmetric about the center of the ROI images. However, the segmented areas of false positives were often shifted away from the center of the ROI images because most of false positives did not have

TABLE I. Features of nodule candidates.

Features based on gray scale and edge gradient (features 1–6)	Mean and standard deviation of the gray scale and mean of the edge gradient of the initial detection area (features 1–3) and the accurately segmented area (features 4–6)
Features based on shape (features 7–26)	Degree of circularity, compactness, area, eccentricity, effective, diameter, the ratio of the length of the minor axis to the length of the major axis of the ellipse that had the same second moments as the region of the nodule candidate, the logarithm of the first three moment invariants, and the maximum absolute value of the Fourier descriptors of the initial detection area (features 7–16) and the accurately segmented area (features 17–26)
Features based on symmetry (features 27–30)	(Features 27 and 28) the symmetry of the shape of the nodule candidate in the vertical and horizontal direction, (features 29–30) the maximum and mean value of features 27 and 28
Features based on location (features 31–33)	(Features 31–33) the horizontal, vertical, and total distances from the center of a nodule candidate to the center of the ROI image

clear and well defined boundaries. Therefore, the symmetry-based features were defined to distinguish between nodules and false positives. First, $Count_{top}$, $Count_{bottom}$, $Count_{left}$, and $Count_{right}$ were calculated to represent the total number of the pixels in the segmented nodule candidate in the top, bottom, left, and right halves of the ROI image, respectively. The following four symmetry-based features were then computed:

$$R_1 = \frac{|Count_{top} - Count_{bottom}|}{Count_{top} + Count_{bottom}}, \quad (1)$$

$$R_2 = \frac{|Count_{left} - Count_{right}|}{Count_{left} + Count_{right}}, \quad (2)$$

$$R_3 = \max(R_1, R_2), \quad (3)$$

$$R_4 = (R_1 + R_2)/2, \quad (4)$$

where R_1 and R_2 represent the symmetry of the shape of nodule candidates in the vertical and horizontal direction, respectively, and R_3 and R_4 represent the maximum and mean value of R_1 and R_2 , respectively. The smaller the four features, the more symmetric the nodule candidate, and the more likely the nodule candidate is a nodule.

II.D.4. Features based on locations of nodule candidates

Three features based on locations of nodule candidates in the small ROI images were determined, and they represented the horizontal, vertical, and total distances between the center of a nodule candidate and the center of the ROI image. The nodule candidate with small distance values was more likely to be a nodule.

II.E. False positive reduction by use of a stepwise linear classifier

A stepwise linear classifier with minimized overtraining effect was employed for false positive reduction.³⁰ Features were first selected based on the ratio of the within-class distance and between-class distance of features for nodules and false positives. The five most selected features were degree of circularity, compactness, eccentricity, effective diameter of the accurately segmented area, and the distance from the center of a nodule candidate to the center of the ROI image. A linear classifier was then used to classify the nodule candidates into nodules and false positives. For the output of the classifier, an “optimal” threshold was employed to remove some nodules and many false positives for minimizing the overtraining effect.³¹ Finally, the remaining nodule candidates were input into the linear classifier again, and the above steps were repeated until an expected sensitivity was reached.

The above four sections comprise the conventional CAD scheme, and the output of the classifier indicated the nodule candidates detected by the conventional CAD scheme. We added the following two steps to construct the fusion CAD scheme.

II.F. Registration of the nodule candidates

Given our image acquisition geometry, a nodule in the three projection images of a subject should have the same



(a)



(b)



(c)

Fig. 6. Three multiprojection images (a) at 3° , (b) 0° (posterior anterior), and (c) -3° .

y-coordinate but different x-coordinate. The coordinates of the centers of a real nodule in the three images in Fig. 6 were (412, 303), (428, 303), (449, 303). Therefore, the difference in the x-coordinate between the three images was quite large. To reduce the large difference in x-coordinate of a nodule in the three images, we registered and shifted the two images at $\pm 3^\circ$ with respect to the PA image.

We first corrected the difference in x -coordinate for nodule candidates by registering the image at oblique view of 3° with the PA image. The central half of the PA image was cut out and considered as the template image, which included most of the lung area and a small part of nonlung area. According to the imaging principles, the image at 3° should be shifted to the left of the PA image by 5–25 pixels, depending on the distance between the object to be imaged and the x-ray detector. Therefore, the image at 3° was moved rightward for 5–25 pixels, and thus obtained 21 search images (the central half of the shifted image at 3°) with the same size as the template image. The absolute difference in pixel value between each of the 21 search images and the template image was then calculated. The search image with the minimal absolute difference was considered as the “optimal” search image registered with the template image, and the shift value of the optimal search image was deemed as the offset value of the image at 3° . Finally, the image at 3° was translated by the offset value to register it with the PA image. We also registered the image at -3° with the PA image by using a similar method.

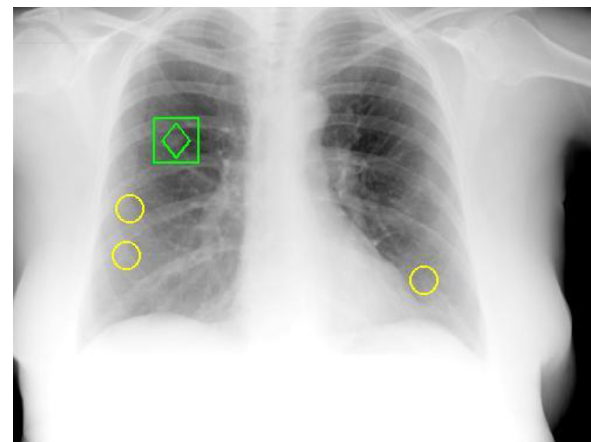
After the registration of the two projection images, the lung areas were well matched, but the horizontal location of a nodule in the two images could still differ by a small amount, depending on the distance between the nodule and the flat-panel x-ray detector. Taking into account of this small difference and errors caused by noise, the permissible error ranges in the x - and y -coordinate for registering a nodule candidate in the two matched images were set to 10 pixels (7.8 mm) and 5 pixels (3.9 mm), respectively. We then used these permissible error ranges to find registered nodule candidates in the two projection images.

Specifically, for a nodule candidate at location (x,y) in the PA image, if there was no nodule candidate in a rectangular area of 20×10 pixels centered at (x,y) in the translated image at 3° , the nodule candidate in the PA image would have no matching nodule candidate; if there was a single nodule candidate in the rectangular area, the two nodule candidates were considered as the same one in the two images; if there were more than one nodule candidate in the rectangular area, all of them were potential matching nodule candidates. Therefore, one candidate was randomly selected as the registered one, and the other nodule candidates would be used to match with remaining nodule candidates.

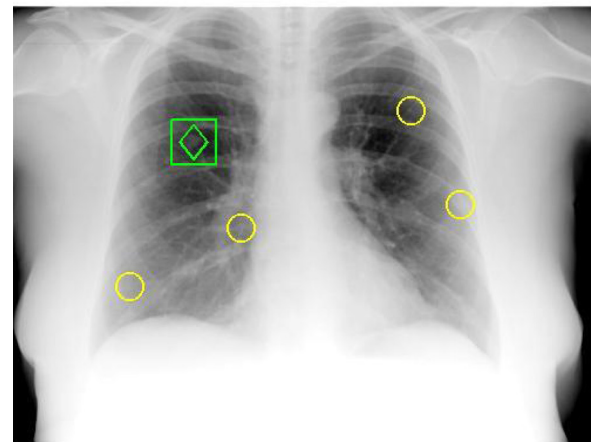
In this study, we first registered the detected nodule candidates in the PA image with the nodule candidates in the images at 3° and -3° , and then registered the nodule candidates in the two images at $\pm 3^\circ$.

II.G. False positive reduction by use of correlation information between nodule candidates

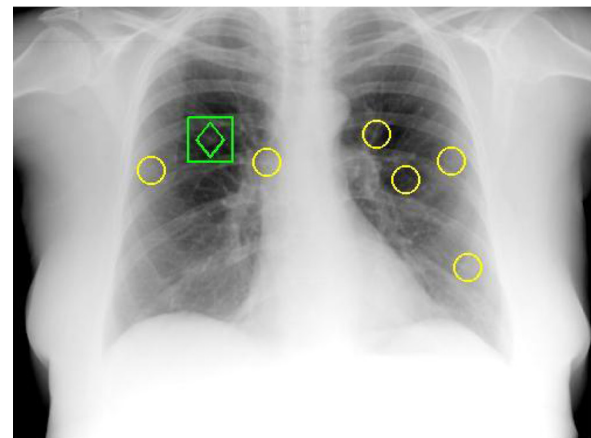
After the registration, a nodule candidate could be detected once, twice, or three times in the three images. If a nodule candidate was detected more than once in the three images of a subject, it was retained as a “true” nodule. Otherwise, it was removed as a false positive.



(a)



(b)



(c)

Fig. 7. Nodule detection results of the conventional CAD scheme for a patient in (a) the image of 3° , (b) PA image, and (c) image of -3° . The circles and squares represent the nodule candidates detected only once and more than once, respectively, by the conventional CAD scheme, and the diamonds indicates the true nodule. On average, there were 4.3 false positives (circles) in each image reported by the conventional CAD scheme; all these false positives were removed by the integration of correlation information between the nodule candidates in the three projection images.

Figure 7 shows the detection result of the conventional CAD scheme in the three projection images of a patient at the 60% sensitivity. The circles and squares represent the

nodule candidates detected only once and more than once, respectively, by the conventional CAD scheme, and the diamonds indicates the true nodule. On average, there were 5.3 nodule candidates (including 4.3 false positives) in each image reported by the conventional CAD scheme; however, when the correlation information between the three images was employed, only one candidate (the true nodule indicated by the diamonds) was reported as nodules by the fusion CAD scheme. It is apparent that integrating correlation information between the nodule candidates in the three images would significantly improve the detection performance of the fusion CAD scheme.

II.H. Evaluation methodologies

The registration of the three images of a patient was a critical step for the fusion CAD scheme. In this study, we employed the percentage error in the pixel value between the two registered images f_1 and f_2 to evaluate the accuracy of the registration algorithm as follows:

$$E = \frac{\frac{1}{nm} \sum_{x=1,2,\dots,n,y=1,2,\dots,m} |f_1(x,y) - f_2(x,y)|}{\frac{1}{2nm} \sum_{x=1,2,\dots,n,y=1,2,\dots,m} |f_1(x,y)| + |f_2(x,y)|} \times 100\%, \quad (5)$$

where m and n are the width and height of the two images, respectively. A large percentage error value indicates a poor registration.

The performance of our CAD schemes for nodule detection was evaluated by comparing the computer-identified locations with the predetermined locations of the centers of nodules. If the distance between the center of a candidate and that of a true nodule was less than 15 pixels (11.6 mm), the nodule was considered as a detected one; otherwise, it was considered as one missed by the CAD schemes. The distance of fifteen pixels (11.6 mm) above was empirically selected based on our experience in lung nodule detection. It is important to note that, in addition to using this fixed threshold of 15 pixels, we have visually confirmed whether each true nodule was indeed detected by the fusion CAD.

A leave-one-subject-out method was employed to evaluate the performance of our CAD schemes. The three images of a subject were selected as test images, and the images of other 58 subjects were used to train our CAD schemes. The trained CAD schemes were then applied to the three selected test images for detecting nodule candidates. This process was repeated 59 times, each for a specific subject, to conclude the leave-one-subject-out evaluation method.

The performance levels of our CAD schemes were measured with a free-response receiver operating characteristic (FROC) curve.³² The number of false positives per images at the three detection sensitivities 70%, 65%, and 60% were also reported.

III. RESULTS

III.A. Result for image registration

Figure 8 shows the percentage errors for the registration algorithm for all 59 subjects. For the percentage errors

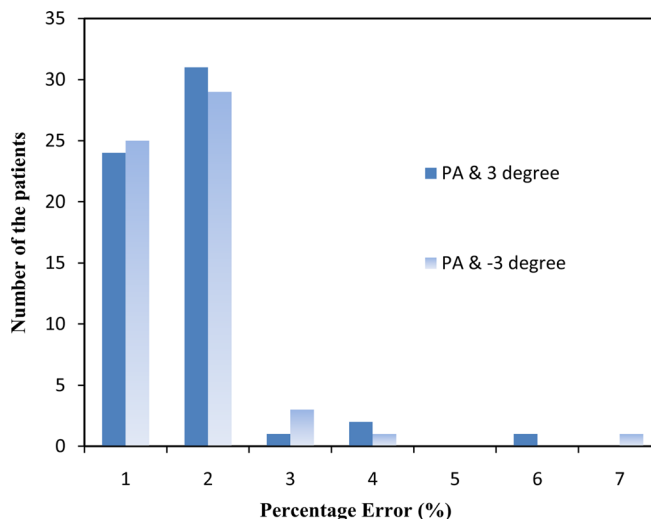


FIG. 8. Number of patients with different levels of percentage error for image registration between PA image and images at oblique angles of 3° and -3° in 59 patients.

between the PA image and the image at 3°, 24, 31, 1, 2, and 1 patients were in the ranges of [0%, 1%], [1%, 2%], [2%, 3%], [3%, 4%], and >5%, respectively. For the percentage errors between the PA image and the image at -3°, 25, 29, 3, 1, and 1 patients were in the above ranges. The percentage errors for 92.4% subjects were below 2%. This ensures the correct registration of nodule candidates in the three images as well as a good performance for the fusion CAD scheme.

III.B. Performance of initial identification of nodule candidates

Table II shows how the decrement value of the threshold for initial nodule identification affects the performance of initial nodule detection in Sec. II B. A small decrement value generally leads to a high detection sensitivity and a large number of false positives. In order to achieve a high sensitivity, we set the decrement value to 5, at which 96.3% nodules were detected along with 216.4 false positives per image.

III.C. Performance of the conventional and fusion CAD schemes

Figure 9 shows the FROC curves of our conventional and fusion CAD schemes. Compared with the conventional CAD scheme, the fusion CAD scheme markedly improved the

TABLE II. The relationship between the decrement of threshold and the performance of initial nodule detection.

Decrement of threshold	Sensitivity (%)	Number of false positives per image
5	96.3	216.4
10	94.1	199.1
15	91.1	183.2
20	91.9	170.6
25	88.9	156.1
30	85.2	144.9

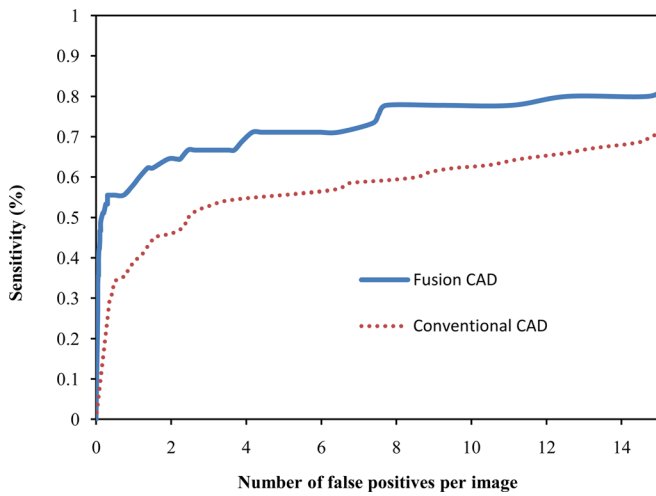


FIG. 9. FROC curves of the conventional CAD scheme and fusion CAD scheme. By integrating correlation information in multiprojection chest radiology, the performance of the fusion CAD scheme was markedly improved over that of the conventional CAD scheme.

performance of nodule detection. Table III indicates that at the sensitivities of 70%, 65%, 60%, our conventional CAD scheme reported 14.7, 11.3, and 8.6 false positives per image, respectively, whereas our fusion CAD scheme significantly reduced the number of false positives to 3.9, 1.9, and 1.2 per image, and 5.5, 2.8, and 1.7 false positives per patient, respectively.

IV. DISCUSSION

A low sensitivity and a large number of false positives are main issues of current CAD schemes for nodule detection in chest radiography. It is more so if the nodules to be detected are small and of low contrast. These issues have severe negative impact on clinical application of CAD schemes. In this study, we developed a new fusion CAD scheme to markedly improve the performance of nodule detection by use of the correlation information between the nodule candidates detected by the conventional CAD scheme. To our knowledge, this is the first study of its kind in the field of computer-aided diagnosis.

Because the nodules were real target objects for our conventional CAD scheme, they were more likely to be detected multiple times in the multiprojection chest radiography than non-nodules. Therefore, the true nodules had strong correlation information, and they were more likely to be retained as nodules by our fusion CAD scheme. On the other hand, the

false positives were caused by either noise or non-nodule objects, and they were less likely to be detected multiple times in the multiprojection chest radiography. Therefore, the false positives had weak correlation information, and they were more likely to be removed as false positives by our fusion CAD scheme, as shown in Fig. 7.

We compared the detection performance levels of the fusion CAD for real and simulated nodules. At the overall sensitivities of 71.1%, 66.7%, and 60.0%, the fusion CAD scheme detected 3 of 7 real nodules; and 29, 27, and 24 of 38 simulated nodules, respectively. Please note that the detection rate for real nodule was quite low because the CAD scheme was primarily trained with simulated nodules and real nodules had very limited impact on the training of the CAD scheme. The only effective way to improve the detection rate for real nodules is to markedly increase the number of real nodules for training, which is an impractical task for this preliminary study.

We analyzed all false positives reported by the fusion CAD scheme at the sensitivity of 70%. We found that the main sources of false positives were ribs (40%), blood vessels (40%), intercostal (inter-rib) space mainly caused by random noise (18%) and soft tissue in mediastinum (2%).

In order to have as many nodules registered in different views as possible, we registered the nodule candidates using location information only. We verified that none of the true nodules was incorrectly removed by use of this registration method (i.e., all true nodules were registered correctly). We also found that when the sensitivity of the fusion CAD scheme was set at 75%, only three false positives in one view were matched to multiple false positives in other views. Therefore, this simple nodule registration method seems to be a good one, and adding other information such as nodule size to the registration method would have minimal effect on the performance of the fusion CAD scheme.

In this study, we used three projection images from each subject. If we used more projection images from each subject, we should have achieved a higher performance level for our fusion CAD scheme, because nodules have stronger correlation in multiprojection images than false positives. However, an increase in the number of projection images would lead to an increase in radiation dose to subjects.

The high noise level, along with the small size and low contrast of the nodules, would be the three primary reasons for the low performance of our conventional CAD scheme. The radiation dose for acquiring each of the three projection images was a third of that for acquiring a standard PA radiography. Therefore, the noise level is higher in the multiprojection radiography than in regular PA radiography. The mean diameter of the nodules in this study was 6.4 mm, which is much smaller than the mean diameter (17 mm) of the nodules in a public database³³ that was used by many existing CAD schemes.¹²⁻¹⁷ The contrast of the simulated nodules ranged from 5% to 15%.

Due to the small number of real nodules, many simulated nodules were used to train and test our CAD schemes. We randomly added the simulated nodules into the images of different patients, and adjusted the size and contrast of the

TABLE III. The performance of nodule detection of the conventional CAD scheme and the fusion CAD scheme.

	Sensitivity		
	70%	65%	60%
Number of false positives for conventional CAD scheme	14.7/image	11.3/image	8.6/image
Number of false positives for fusion CAD scheme	3.9/image	1.9/image	1.2/image
	5.5/patient	2.8/patient	1.7/patient

simulated nodules. Although the images themselves were the real chest images of patients, and the shape, gray scale, and contrast of simulated nodules were similar to those of real nodules, the readers should be aware that the performance levels achieved in this study may be quite different from the performance levels if real nodules were used. However, we strongly believe that, if we used real nodules rather than simulated nodules to train and test our CAD schemes, the conclusion of this study would not change; that is, the performance of nodule detection can be markedly improved by use of correlation information between the registered nodule candidates in multiprojection images.

V. CONCLUSIONS

In this study, we developed a conventional CAD scheme and a fusion CAD scheme for lung nodule detection in multiprojection chest radiography. The fusion CAD scheme registered the nodule candidates in multiprojection images, and markedly removed the false positives by use of correlation information between the registered nodule candidates. Compared with the conventional CAD scheme, the fusion CAD scheme achieved a markedly higher performance for nodule detection.

ACKNOWLEDGMENTS

This work was supported by USPHS Grant No. R01 CA113870. CAD technologies developed by Qiang Li, Junji Shiraishi, Kunio Doi, and their colleagues have been licensed to companies including Hologic, Inc., Riverain Medical Group, Median Technology, Mitsubishi Space Software Co., General Electric Corporation, and Toshiba Corporation. K.D. is shareholder in Hologic, Inc., Los Altos, CA. It is the policies of Duke University and The University of Chicago that investigators disclose publicly actual or potential significant financial interests that may appear to be affected by research activities.

^{a)}Author to whom correspondence should be addressed. Electronic mail: li.qiang@duke.edu

¹A. Jemal, R. Siegel, J. Xu, and E. Ward, "Cancer statistics, 2010," *Ca-Cancer J. Clin.* **60**(5), 277–300 (2010).

²C. I. Henschke, D. F. Yankelevitz, D. M. Libby, M. W. Pasmantier, J. P. Simth, and O. S. Miettinen, "The International Early Lung Cancer Action Program Investigators: Survival of patients with stage I lung cancer detected on CT screening," *N. Engl. J. Med.* **355**(17), 1763–1771 (2006).

³F. O. Bochud, F. R. Verdun, C. Hessler, and J. F. Valley, "Detectability on radiological images—The influence of anatomical noise," *Proc. SPIE* **2436**, 156–164 (1995).

⁴E. Samei, M. J. Flynn, and W. R. Eyer, "Detection of subtle lung nodules: Relative influence of quantum and anatomic noise on chest radiographs," *Radiology* **213**, 727–734 (1999).

⁵The National Lung Screening Trial Research Team, "Reduced lung-cancer mortality with low-dose computed tomographic screening," *N. Engl. J. Med.* **365**(5), 395–409 (2011).

⁶J. L. Mulshine and D. C. Sullivan, "Clinical practice. Lung cancer screening," *N. Engl. J. Med.* **352**(26), 2714–2720 (2005).

⁷J. T. Dobbins III and D. J. Godfrey, "Digital x-ray tomosynthesis: Current state of the art and clinical potential," *Phys. Med. Biol.* **48**(19), 65–106 (2003).

⁸J. T. Dobbins III and H. P. McAdams, "Chest tomosynthesis: Technical principles and clinical update," *Eur. J. Radiol.* **72**(2), 244–251 (2009).

⁹E. Samei, S. A. Stebbins, J. T. Dobbins III, and J. Y. Lo, "Multiprojection correlation imaging for improved detection of pulmonary nodules," *AJR, Am. J. Roentgenol.* **188**(3), 1239–1245 (2007).

¹⁰A. S. Chawla, S. Boyce, L. Washington, H. P. McAdams, and E. Samei, "Design and development of a new multi-projection x-ray system for chest imaging," *IEEE Trans. Nucl. Sci.* **56**(1), 36–45 (2009).

¹¹E. Samei, D. M. Catarious, A. H. Baydush, C. E. Floyd, and R. Vargas-Voracek, "Bi-plane correlation imaging for improved detection of lung nodules," *Proc. SPIE* **5030**, 284–297 (2003).

¹²G. Coppomo, S. Diciotti, M. Falchini, N. Villari, and G. Valli, "Neural networks for computer-aided diagnosis: Detection of lung nodules in chest radiographs," *IEEE Trans. Inf. Technol. Biomed.* **7**(4), 344–357 (2003).

¹³A. M. R. Schilham, B. van Ginneken, and M. Loog, "A computer-aided diagnosis system for detection of lung nodules in chest radiographs with an evaluation on a public database," *Med. Image Anal.* **10**(20), 247–258 (2006).

¹⁴P. Campadelli, E. Casiraghi, and D. Artioli, "A fully automated method for lung nodule detection from postero-anterior chest radiographs," *IEEE Trans. Med. Imaging* **25**(12), 1588–1603 (2006).

¹⁵J. Shiraishi, H. Abe, F. Li, R. Engelmann, H. MacMahon, and K. Doi, "Computer-aided diagnosis for the detection and classification of lung cancers on chest radiographs ROC analysis of radiologists' performance," *Acad. Radiol.* **13**(8), 995–1003 (2006).

¹⁶R. C. Hardie, S. K. Rogers, T. Wilson, and A. Rogers, "Performance analysis of a new computer aided detection system for identifying lung nodules on chest radiographs," *Med. Image Anal.* **12**(3), 240–258 (2008).

¹⁷S. Chen, K. Suzuki, and H. MacMahon, "Development and evaluation of a computer-aided diagnostic scheme for lung nodule detection in chest radiographs by means of two-stage nodule enhancement with support vector classification," *Med. Phys.* **38**(4), 1844–1858 (2011).

¹⁸B. van Ginneken, B. M. H. Romeny, and M. A. Viergever, "Computer-aided diagnosis in chest radiography: A survey," *IEEE Trans. Med. Imaging* **20**(12), 1228–1241 (2001).

¹⁹Q. Li, S. Katsuragawa, and K. Doi, "Computer-aided diagnostic scheme for lung nodule detection in digital chest radiographs by use of a multiple-template matching technique," *Med. Phys.* **28**(10), 2070–2076 (2001).

²⁰K. Suzuki, J. Shiraishi, H. Abe, H. MacMahon, and K. Doi, "False-positive reduction in computer-aided diagnostic scheme for detecting nodules in chest radiographs by means of massive training artificial neural network," *Acad. Radiol.* **12**(2), 191–201 (2005).

²¹J. Shiraishi, Q. Li, K. Suzuki, R. Engelmann, and K. Doi, "Computer-aided diagnostic scheme for the detection of lung nodules on chest radiographs: Localized search method based on anatomical classification," *Med. Phys.* **33**(7), 2642–2653 (2006).

²²D. W. De Boo, M. Prokop, M. Uffmann, B. van Ginneken, and C. M. Schaefer-Prokop, "Computer-aided detection (CAD) of lung nodules and small tumours on chest radiographs," *Eur. J. Radiol.* **72**, 218–225 (2009).

²³E. Samei, M. J. Flynn, and W. R. Eyer, "Detection of subtle lung nodules: Relative influence of quantum and anatomical noise on chest radiographs," *Radiography* **213**, 727–734 (1999).

²⁴B. D. Alessandro, M. Madsen, E. Samei, X. Li, J. Wooi-Tan, K. S. Berbaum, K. Schartz, R. Caldwell, and L. S. Zuckier, "Synthetic positron emission tomography-computed tomography images for use in perceptual studies," *Semin Nucl Med.* (in press).

²⁵X. Xu and K. Doi, "Image feature analysis for computer-aided diagnosis: Accurate determination of ribcage boundary in chest radiographs," *Med. Phys.* **22**(5), 617–626 (1995).

²⁶X. Xu and K. Doi, "Image feature analysis for computer-aided diagnosis: Detection of right and left hemidiaphragm edges and delineation of lung field in chest radiographs," *Med. Phys.* **23**(9), 1613–1624 (1996).

²⁷M. Aoyama, Q. Li, S. Katsuragawa, F. Li, S. Sone, and K. Doi, "Computerized scheme for determination of the likelihood measure of malignancy for pulmonary nodules on low-dose CT images," *Med. Phys.* **30**(3), 387–394 (2003).

²⁸J. Wang, R. Engelmann, and Q. Li, "Segmentation of pulmonary nodules in three-dimensional CT images by use of a spiral-scanning technique," *Med. Phys.* **34**(12), 4678–4689 (2007).

²⁹R. C. Gonzalez, R. E. Woods, and S. L. Eddins, *Digital Image Processing Using MATLAB* (Prentice-Hall, Englewood Cliffs, New Jersey, 2003).

³⁰Q. Li, F. Li, and K. Doi, "Computerized detection of lung nodules in thin-section CT images by use of selective enhancement filters and an automated rule-based classifier," *Acad. Radiol.* **15**(12), 165–175 (2008).

- ³¹Q. Li and K. Doi, "Analysis and minimization of overtraining effect in rule-based classifiers for computer-aided diagnosis," *Med. Phys.* **33**(2), 320–328 (2006).
- ³²C. E. Metz, "Some practical issues of experimental design and data analysis in radiological ROC studies," *Invest. Radiol.* **24**(3), 234–245 (1989).
- ³³J. Shiraishi, S. Katsuragawa, J. Ikezoe, T. Matsumoto, T. Kobayashi, K. Komatsu, M. Matsui, H. Fujita, Y. Kodera, and K. Doi, "Development of a digital image database for chest radiographs with and without a lung nodule: Receiver operating characteristic analysis of radiologists' detection of pulmonary nodules," *AJR, Am. J. Roentgenol.* **174**(1), 71–74 (2000).